Vortical versus skyrmionic states in mesoscopic *p*-wave superconductors

V. Fernández Becerra,[1] E. Sardella,[2] F. M. Peeters,[1] and M. V. Milošević[1,*]

[1]*Departement Fysica, Universiteit Antwerpen, Groenenborgerlaan 171, B-2020 Antwerpen, Belgium*

[2]*UNESP-Universidade Estadual Paulista, Departamento de Física, Faculdade de Ciências,*
Caixa Postal 473, 17033-360 Bauru, São Paulo, Brazil

We investigate the superconducting states that arise as a consequence of mesoscopic confinement and a multicomponent order parameter in the Ginzburg-Landau model for *p*-wave superconductivity. Conventional vortices, but also half-quantum vortices and skyrmions, are found as the applied magnetic field and the anisotropy parameters of the Fermi surface are varied. The solutions are well differentiated by a topological charge that for skyrmions is given by the Hopf invariant and for vortices by the circulation of the superconducting velocity. We revealed several unique states combining vortices and skyrmions, their possible reconfiguration with varied magnetic field, as well as temporal and field-induced transitions between vortical and skyrmionic states.

I. INTRODUCTION

Strontium ruthenate, Sr_2RuO_4, is according to theoretical predictions the best candidate to date to host *p*-wave superconductivity. Generally speaking, the order parameter in superconductors describes the spatial profile of the gap function, $\Delta_{ij}(k)$. The order parameter in *p*-wave superconductivity is an odd function of the wave vector **k**, unlike the *s*-wave superconductors where it is an even function of **k** [1]. Following the notation of Balian and Werthamer, the *p*-wave order parameter reads [2,3]

$$\hat{\Delta}(k) = \begin{bmatrix} -d_x(k) + id_y(k) & d_z(k) \\ d_z(k) & d_x(k) + id_y(k) \end{bmatrix}, \quad (1)$$

or in a short notation $\hat{\Delta}(k) = i\,[\vec{d}(k) \cdot \hat{\sigma}]\,\sigma_y$, where $\vec{d}(k)$ transforms as a vector under rotations and σ_i are Pauli matrices. Microscopic calculation of the superconducting gap is a highly demanding task that requires a detailed knowledge of the pairing mechanism which in many cases is not available. What remains then is to exploit all the symmetries (continuous and discrete) exhibited by the material under consideration and build a model that will depend on a certain number of parameters. The possible superconducting order parameters that have been reported for *p*-wave superconductors required a detailed description of the crystal structure of the considered material [2,3]. In that respect, strontium ruthenate (SRO) is a layered perovskite with a crystal structure similar to the well-known high-T_c superconductor $(La,Sr)_2CuO_4$, where oxygen ions at the corners of an octahedron surround the body-centered Ru ion [1,4]. The planar layers of RuO_2 are separated by Sr layers that stack along the highly symmetric axis *c*. The Fermi surface of strontium ruthenate contains three sheets arising from the binding of the Ru and O ions within the same layer [5]. Bindings between the RuO_2 layers are weak due to the long separation of the interplanar RuO_6 octahedra. The Fermi sheets α and β are both one dimensional (1D), while the γ sheet is two dimensional (2D). A rigorous analysis found that among the five irreducible representations for vector $\vec{d}(k)$ in the lattice point group

D_{4h}, there are four 1D, $\vec{d} = k_x\hat{\mathbf{x}} \pm k_y\hat{\mathbf{y}}$ and $\vec{d} = k_y\hat{\mathbf{x}} \pm k_x\hat{\mathbf{y}}$, and one 2D, $\vec{d} = (k_x \pm ik_y)\hat{\mathbf{z}}$, representations [2,3]. These 1D and 2D representations, namely helical and chiral, are the electronic analogs of the *B* and *A* phases of the superfluid ^{3}He [2], respectively. Knight-shift measurements were not able to discern the chiral from the helical contributions, since they detected constant spin susceptibility (χ_c) for external field either within the RuO_2 plane or perpendicular to it [6,7]. On the other hand, muon-spin relaxation (μSR) and the optical Kerr effect experiments have detected spontaneous magnetic fields [8,9], only possible in the chiral phase that breaks the time-reversal symmetry (TRS) [10].

To confirm or discard SRO as a chiral superconductor, magnetic response experiments have been carried out on single crystals, but have failed to convincingly detect the spontaneous currents predicted to exist in chiral domain walls and close to sample edges [11–13]. In these works, numerical simulations of evenly distributed chiral domains estimated a minimal domain-wall length of 2 μm $\approx 30\xi_0$ (where ξ_0 is the zero-temperature coherence length of SRO) to be detectable in a scanning superconducting quantum interference device (SQUID) setup. Such domains are energetically costly in a bulk system, but are likely to stabilize in a mesoscopic sample of comparable size.

Therefore, to provide further insights in chiral physics of *p*-wave superconductors [14–16], in this work we employ the chiral *p*-wave Ginzburg-Landau (GL) model [3,17–19], to report distinct mesoscopic effects of chirality in the superconducting state and related experimental observables, which in turn can serve to discriminate chiral from helical contributions in superconductors like SRO. We report the stabilization of various topological entities, full vortex (FV), half-quantum vortex (HQV), and skyrmion states. Skyrmion states, carrying topological charge defined by the Hopf invariant [20,21], are one of the distinct hallmarks of chiral superconductivity, and can be stable in bulk *p*-wave superconductors [21]. It is well known in conventional *s*-wave superconductivity that confinement can stabilize superconducting configurations which in bulk systems are energetically unfavorable or even unattainable, e.g., non-Abrikosov vortex lattices, or vortices with phase winding $\phi = 2\pi n$, with $n > 1$ (giant vortices)

*Milorad.Milosevic@uantwerpen.be

[22]. In mesoscopic spin-triplet superconductors HQVs have been predicted to exist, owing the reduction of their otherwise divergent energy to the low dimensionality of the system [23]. They carry unscreened spin currents and half the vorticity of a full vortex [23,24]. Despite the fact that in the chiral phase vector $\vec{d}$ is locked to the $\hat{z}$ axis [3,19], we found analogous HQVs defined by (i) the 2π-phase winding of one of the chiral superconducting components, and (ii) the anisotropic screening that causes their attraction to the edges of the mesoscopic sample. We present the found HQV states in multiple forms, but also FV and skyrmionic states and transitions between them as a function of the external magnetic field applied perpendicularly to the sample. We employed the time-dependent theoretical formalism, which allowed us to observe temporal transitions as well, related to peculiar entry and arrangement of HQVs and their temporal transformations into other topologies. The HQVs that were found to reside at the sample edges are the realization of the quasi-1D periodic array of domains discussed in Ref. [12].

The paper is organized as follows. Section II presents the theoretical formalism and our analytical analysis of the first GL equation and the superconducting current. The boundary conditions imposed on our equations are derived from the latter expression. Section III then summons our findings for the superconducting configurations composed of HQV, FV, and skyrmion states, obtained at weak coupling and considering a cylindrical Fermi surface. The transitions between states of interest as a function of the magnetic field are discussed in Sec. IV, while the temporal transformations are shown in Sec. V. The effect of anisotropy on the topological, vortical, and skyrmionic entities is analyzed in Sec. VI. Our findings and conclusions are summarized in Sec. VII.

II. THEORETICAL FORMALISM

After the above brief general description of strontium ruthenate, in what follows we show the Ginzburg-Landau (GL) equations that the order parameter, $\vec{\Psi} = (\psi_x, \psi_y)^T$, must satisfy. The order parameter has two components (is chiral) as

a consequence of the two-dimensional representation ($\Gamma_5^\pm$) of the tetragonal group D_{4h} [3]. The expansion of the GL free energy density up to fourth order in $\psi_{x,y}$, that fulfills the group symmetries, reads

$$
\begin{aligned}
\mathscr{F} ={}& K(|D_x\psi_x|^2 + |D_y\psi_y|^2) + k_1(|D_x\psi_y|^2 + |D_y\psi_x|^2) \\
&+ 2\,\mathrm{Re}\{k_2 D_x\psi_x (D_y\psi_y)^* + k_3 D_x\psi_y (D_y\psi_x)^*\} - \alpha|\vec{\Psi}|^2 \\
&+ \beta_1|\vec{\Psi}|^4 + \beta_2(\psi_x^*\psi_y - \psi_x\psi_y^*)^2 + \beta_3|\psi_x|^2|\psi_y|^2,
\end{aligned} \quad (2)
$$

where α, k_i, and β_i, with $i = 1,2,3$, are parameters that depend on the details of the Fermi surface of the material under consideration. $K = \sum_i k_i$ and $D_{x,y}$ denote the components of the covariant derivative. The time-dependent Ginzburg-Landau (TDGL) equations, used in our numerical approach [25], are the set of coupled differential equations for the superconducting order parameter $\vec{\Psi}$ and the vector potential $\vec{A}$ [26],

$$
\frac{\hbar^2}{2m_s D}\left(\frac{\partial}{\partial t} + \frac{2ie}{\hbar}\varphi\right)\vec{\Psi} = -\frac{\delta\mathscr{F}}{\delta\vec{\Psi}^*}, \quad (3)
$$

$$
\frac{\sigma}{c}\left(\frac{1}{c}\frac{\partial\vec{A}}{\partial t} + \vec{\nabla}\varphi\right) = -\frac{\delta\mathscr{F}}{\delta\vec{A}} - \frac{1}{4\pi}\vec{\nabla}\times\vec{B}, \quad (4)
$$

where φ is the scalar electric potential, $\vec{B}$ is the magnetic induction, m_s is the effective mass, D is the phenomenological diffusion coefficient, and σ is the electrical conductivity. For convenience we set $\hbar = 1$ and $m_s = 1/2$. The second GL equation [Eq. (4)] is discarded in this work since the diamagnetic effects of superconductors are vanishingly small for a thin (effectively 2D) mesoscopic geometry. We use the symmetric gauge for the vector potential, $\vec{A} = (\vec{r}\times\vec{H})/2$, with the magnetic field ($\vec{H}$) directed along $\hat{z}$. The scalar electric potential is set to zero since neither charges nor external currents are considered in this work. In dimensionless units, where distance is scaled to the coherence length, $\xi = \sqrt{\frac{1}{\alpha}}$, time to $t_0 = \frac{\xi^2}{D}$, magnetic field to the upper bulk critical field $H_{c2} = \frac{c}{2|e|\xi^2}$, and the superconducting order parameter to $\Delta_+ = \sqrt{\frac{\alpha}{2\beta_1}}$, the first TDGL equation becomes

$$
\frac{\partial\vec{\Psi}}{\partial t} = \begin{bmatrix} \frac{K+k_1}{2}\vec{D}^2 + \frac{k_2-k_3}{2i}[D_x, D_y] & (k_2+k_3)\,\Pi_+^2 \\ (k_2+k_3)\,\Pi_-^2 & \frac{K+k_1}{2}\vec{D}^2 - \frac{k_2-k_3}{2i}[D_x, D_y] \end{bmatrix}\begin{pmatrix}\psi_+ \\ \psi_-\end{pmatrix} + \vec{\Psi}\left(1 - \frac{1+\tau}{2}|\vec{\Psi}|^2 \pm \frac{\tau}{2}\vec{\Psi}^*\hat{\sigma}_z\vec{\Psi}\right), \quad (5)
$$

where $\Pi_\pm = \frac{1}{\sqrt{2}}(D_x \pm i D_y)$, $\psi_\pm = \psi_x \pm i\psi_y$, $\beta_3 = 0$ [27], and $\tau = \beta_2/\beta_1$. A straightforward calculation reveals the following important result: $[D_x, D_y] = iH$, which leads the operators $\Pi_\pm$ to satisfy the commutator: $[\Pi_+, \Pi_-] = H$. The external magnetic field, being constant, can be factored out from the above commutators, leading to $[\tilde{\Pi}_+, \tilde{\Pi}_-] = 1$, which defines the algebra behind the Landau levels, $\tilde{\Pi}_\pm = \Pi_\pm/\sqrt{H}$. This algebra is defined through the following commutators: $[\hat{N}, \tilde{\Pi}_+] = -\tilde{\Pi}_+$, $[\hat{N}, \tilde{\Pi}_-] = \tilde{\Pi}_-$; where $\hat{N} = \tilde{\Pi}_+\tilde{\Pi}_-$ is the particle number operator. Within the weak-coupling limit and considering a cylindrical Fermi surface (γ sheet), all the k_i parameters are equal to $\langle v_x^2 v_y^2\rangle / \langle v_x^4\rangle =$

$1/3$, where brackets $\langle\rangle$ denote averaging over the Fermi surface [27], and $\tau = 1/2$. For this case the first GL equation reads

$$
\partial_t\vec{\Psi} = \frac{2}{3}[\vec{D}^2 + \Pi_+^2\hat{\sigma}_+ + \Pi_-^2\hat{\sigma}_-]\vec{\Psi} + \vec{\Psi}\left(1 - \frac{3|\vec{\Psi}|^2}{4} \pm \frac{\vec{\Psi}^*\hat{\sigma}_z\vec{\Psi}}{4}\right), \quad (6)
$$

where $\hat{\sigma}_\pm = (\hat{\sigma}_x \pm i\hat{\sigma}_y)/2$ are pseudospin or chiral operators acting on the space span by $\psi_\pm$. Ignoring the nonlinear terms (linearized case), it is straightforward to show that the superconducting order parameter must be of the form

$\vec{\Psi} = (\phi_N, \phi_{N-2})^T$, where ϕ_N is the state corresponding to the Landau level N [17–19,27–29]. Within the superconducting formalism the number N turns out to be the vorticity of the order parameter. Then, one concludes that for chiral p-wave superconductors there is a vorticity difference of 2 between the components of the superconducting order parameter. The full GL equations, i.e., the linearized equation plus the nonlinear terms, are a complicated set of partial differential equations with restricted analytical solutions [27,29]. Therefore, in this work we solve this problem numerically. Due to the mesoscopic dimension of the sample under consideration, proper boundary conditions must be incorporated in the GL equations in order to pose the problem well. In what follows, the superconducting current is calculated for the general case, which includes the specific case where all k_i's are equal to 1/3, and from this expression the boundary conditions for the first GL equation are derived. The superconducting current density, defined as the negative functional derivative of the GL free energy density with respect to the vector potential, for chiral p-wave superconductors, is

$$\vec{J} = \text{Im}\left\{ \frac{K+k_1}{4}(\psi_+^* \vec{D}\psi_+ + \psi_-^* \vec{D}\psi_-) + \frac{k_2+k_3}{2\sqrt{2}}(\vec{\Psi}^*[\Pi_+\hat{\sigma}_+ + \Pi_-\hat{\sigma}_-]\vec{\Psi}\,\hat{\imath}\right.$$
$$\left. + i\,\vec{\Psi}^*[\Pi_+\hat{\sigma}_+ - \Pi_-\hat{\sigma}_-]\vec{\Psi}\,\hat{\jmath}) + \frac{k_2-k_3}{4}\vec{\Psi}^*\hat{S}_y\vec{D}\hat{\sigma}_z\vec{\Psi} \right\}, \tag{7}$$

where $\hat{\imath}, \hat{\jmath}$ form the canonical base in Cartesian coordinates. The set of operators ($\hat{\sigma}_\pm$ and $\hat{\sigma}_z$) act on $\psi_\pm$, while $\hat{S}_y$ acts on $\{\hat{\imath}, \hat{\jmath}\}$. The superconducting current contains mainly three contributions defined by the following factors: $(K+k_1)/4$, $(k_2+k_3)/2\sqrt{2}$, and $(k_2-k_3)/4$. The first one arises from the conventional term $\vec{D}^2$ in Eq. (5), the second one (we name chiral) is due to the internal degree of freedom (chirality) that appears in Eq. (5) in the form of two nondiagonal terms. Finally, the third contribution arises from the diagonal terms ($\pm[D_x, D_y]$) in Eq. (5), and accounts for the chiral polarization introduced by the orbital Zeeman interaction. Within the weak-coupling limit k_2 and k_3 are equal [17,28,29], but if the the density of states [$N(0)$] weakly depends on the energy derivative [$N'(0)$] at the Fermi surface, k_2 and k_3 slightly differ [18]. The boundary conditions imposed on Eq. (5) for our square mesoscopic sample are given as

$$\left. \begin{array}{c} \psi_+ - \psi_- = 0 \\ D_y\psi_+ + D_y\psi_- = 0 \end{array} \right\} \quad \text{at north and south sides,}$$
$$\left. \begin{array}{c} \psi_+ + \psi_- = 0 \\ D_x\psi_+ - D_x\psi_- = 0 \end{array} \right\} \quad \text{at east and west sides.} \tag{8}$$

It is straightforward to show that the boundary conditions of Eq. (8) set the perpendicular current at the edges to zero, i.e., they impose specular reflection in the chiral p-wave superconductor [3,18,28]. It is important to remark also that they are parameter independent, so they provide the proper boundary conditions for Eq. (6) but also for the most general case of Eq. (5). With Eq. (8) we have completed the set of equations needed for the GL description of a chiral p-wave mesoscopic superconductor. Equation (5) is numerically solved using finite differences and the link variables technique of Ref. [26] on a square lattice with mesh grid $h_x = h_y = 0.1$. On the other hand, the temporal derivative is discretized using the Runge-Kutta method of first order. Before concluding this section, we give the reduced expression for the dimensionless free energy, since it allows us to find not only the lowest energy (ground) states but also the stable states with slightly higher energies (metastable states) The free energy reads

$$\frac{F}{F_0} = \frac{1}{2}\int dV\{(1+\tau)|\vec{\Psi}|^4 + \tau(\vec{\Psi}^*\hat{\sigma}_z\vec{\Psi})^2\}, \tag{9}$$

where $F_0 = \Delta_+^2/\xi^2$ is the bulk free energy at zero field.

III. ISOTROPIC CASE (CYLINDRICAL FERMI SURFACE)

The results obtained using Eq. (6) for a square $8\xi \times 8\xi$ sample are summarized in Fig. 1, showing the dimensionless free energy and the vorticity of vector $\vec{\Psi}$ as a function of the external magnetic field H. Figs. 1(b) and 1(c) show the vorticity of the ground states of our superconducting sample, labeled a–j in Fig. 1(a), where $\nu_{+(-)}$ is the vorticity of the component $\psi_{+(-)}$. Note that both ν_+ and ν_- remain constant along the stability curves of each state in Fig. 1(a), and as such are good identification numbers for these states. Contour plots in Fig. 2 show the order parameter $\vec{\Psi}$ corresponding to the ground states a–d. While the left and central columns of Fig. 2 show contour plots of the superconducting density of each component, $|\psi_+|^2$ and $|\psi_-|^2$, respectively, the third column shows the difference between the angular phases of the components, i.e., $\theta_+ - \theta_-$.

The ground state a of Fig. 2 shows one anisotropic vortex in each component, i.e., vorticity $\nu_+ = -1$ in component ψ_+ and $\nu_- = 1$ in component ψ_-. The contour plots of the ground state b in Fig. 2 show the vortex free state in component ψ_+ and the giant vortex [22] with vorticity $\nu_- = 2$ in component ψ_-. The subsequent ground state c has vorticity $\nu_+ = 2$ and $\nu_- = 4$, where $|\psi_-|^2$ contains four vortices close to the corners, meanwhile $|\psi_+|^2$ shows a pronounced depletion around the center of the sample. The corresponding phase difference figure reveals that the depletion in component ψ_+ is a consequence of two vortices and two vortex-antivortex pairs there. The ground state d has six vortices in $|\psi_-|^2$ in full agreement with the vorticity reported in Figs. 1(b) and 1(c) ($\nu_+ = 4$ and $\nu_- = 6$). However, the density $|\psi_+|^2$ fails to convincingly show any signature of a vortex. The vorticity $\nu_+ = 4$ of component ψ_+ is visible in the phase difference Fig. 2(d), where ten discontinuities are found along the edges as a consequence of six vortices from ψ_- and four from ψ_+. Four vortex-antivortex pairs at the center of the sample are also visible in this contour plot, but do not affect the total vorticity.
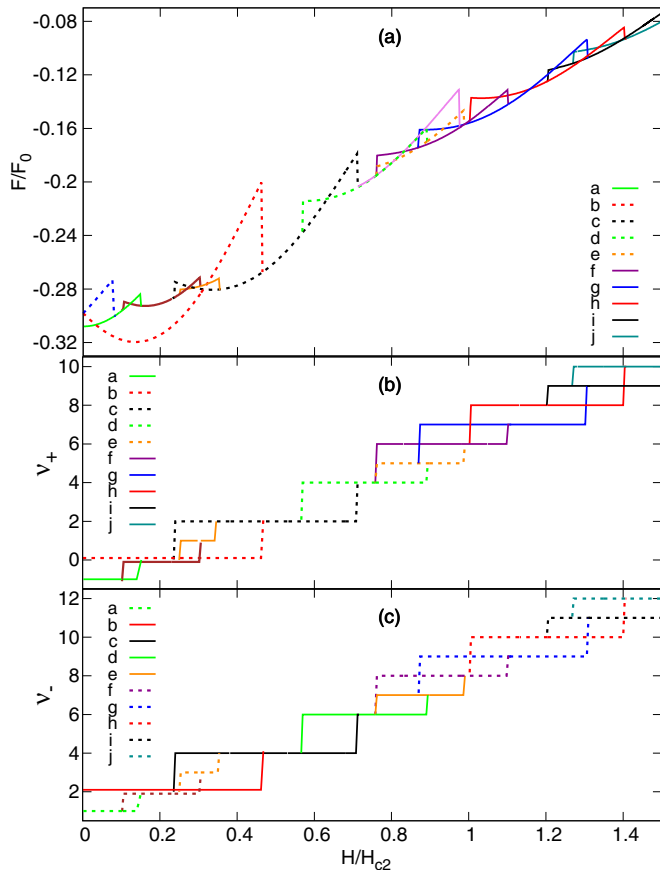
FIG. 1. (a) Free energy in units of the bulk condensation energy at zero field (F_0) as a function of the external magnetic field in units of the bulk upper critical field (H_{c2}), for a square mesoscopic sample of size $8\xi \times 8\xi$. Letter labels denote different found ground states. Some metastable states (not labeled) are also shown in this figure. Vorticity of components ψ_+ and ψ_- of the ground states of panel (a) are shown in (b) and (c) respectively. The difference in vorticity ($\nu_+ - \nu_- = 2$) between the components is in perfect agreement with the analytically predicted solution $\vec{\Psi} = (\phi_N, \phi_{N-2})^T$.

From the comparison between Figs. 2(c) and 2(d) one sees that with increasing the magnetic field the component ψ_- dominates its partner component ψ_+. The dominance of ψ_- over ψ_+, especially at high fields, impedes the proper description of the vortex configuration in the latter component. In order to describe the components of the order parameter on an equal footing, a more suitable representation is in terms of ψ_x and ψ_y. Figures 3 and 4 show contour plots of $|\psi_x|^2$, $|\psi_y|^2$, and $\cos(\theta_x - \theta_y)$ for ground states $a-j$ of Fig. 1. Figure 3(a) shows $\cos(\theta_x - \theta_y)$ for ground state a (from now on called the phase difference figure), and reveals a linear domain wall. Its extension across the sample coincides with the stripe where density $|\psi_y|^2$ vanishes. On the other hand, the partner component ψ_x is free of vortices. Ground states b and c look similar in both densities, although from the comparison between their phase difference figures in Fig. 3(b) and 3(c) respectively, we see four domain walls in state c and none in state b. The domain walls (DWs) of ground state c define a path where the difference between the angular phases of components ψ_x and ψ_y are 0 or π, i.e., $\theta_x - \theta_y = 0, \pi$. Ground
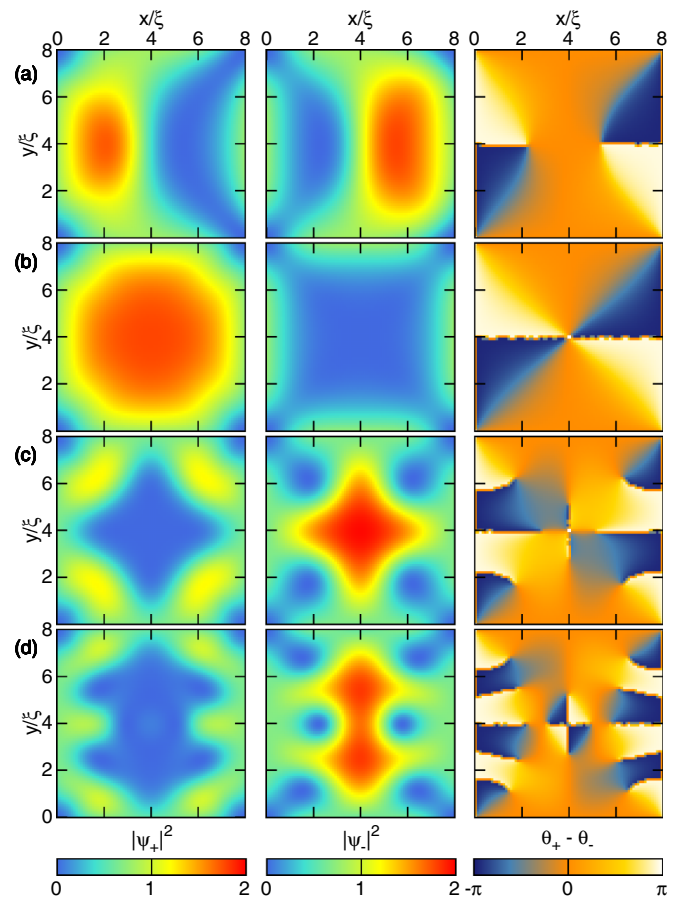

FIG. 2. Ground states $a-d$ of Fig. 1. Left and central columns show the contour plots of the superconducting densities components $|\psi_+|^2$ and $|\psi_-|^2$, respectively. Right column shows the difference between the angular phases of the components, i.e., $\theta_+ - \theta_-$.

state d shows two vortices in density $|\psi_x|^2$ and none in $|\psi_y|^2$, while its corresponding phase difference figure shows the four domain walls of ground state c plus two other alternating domain walls that weakly connect the former ones. The contour plots of Fig. 3(e) for state e show clearly two vortices in each component. They look indistinguishable just from the analysis of their densities, but their phase difference figure reveals that there are two vortices, one in each component, that combine to produce a different signature from the remaining vortices. While the uncorrelated vortices lead to the formation of the alternating domain walls towards sample edges, the pair of correlated vortices align their cores and do not show any domain wall between them. The alternating domain wall is therefore the signature of a half quantum vortex (HQV) defined by the 2π-phase winding of one of its superconducting components, in contrast to the other signature without domain wall that corresponds to the full vortex (FV).

Figure 4 shows the remaining ground states $f-j$ of Fig. 1. Both densities in ground state f clearly show two vortices in each component, which are indeed four HQVs according to the corresponding phase difference figure. Ground states g and h show one common feature, having a different number of vortices per component, but all of them aligned vertically in component ψ_x and horizontally in component ψ_y. On the
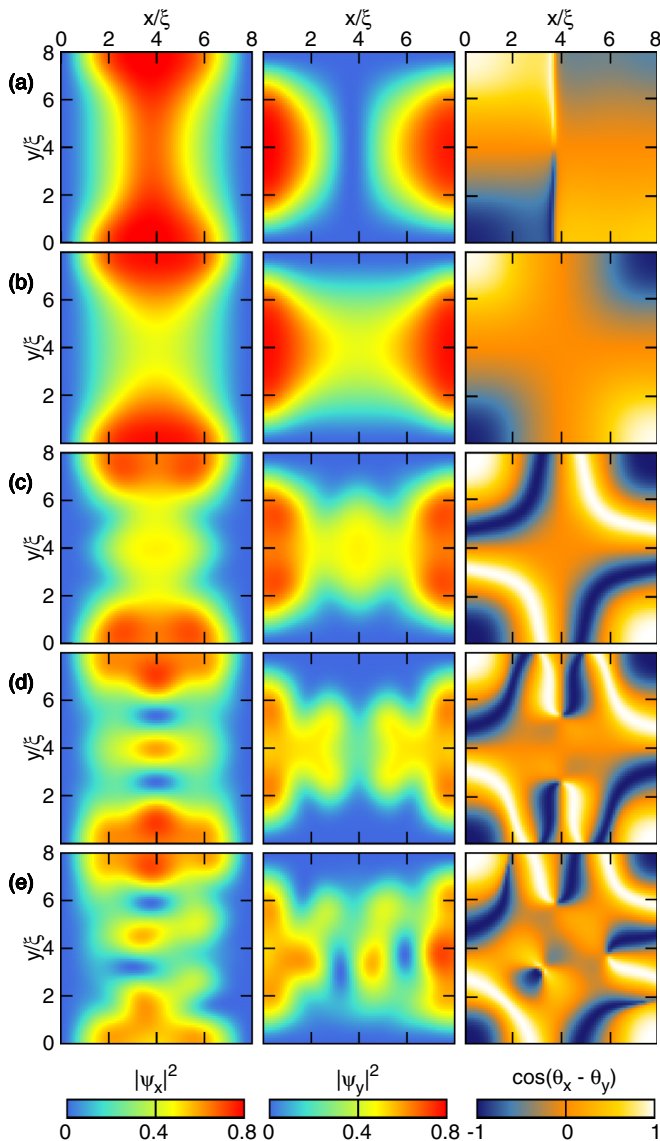
FIG. 3. Ground states $a-e$ of Fig. 1, plotted correspondingly in panels (a)–(e). Left and central columns show the contour plots of the superconducting densities components $|\psi_x|^2$ and $|\psi_y|^2$, respectively. Right column shows $\cos(\theta_x - \theta_y)$, where $\theta_{x,y}$ are the angular phases of components ψ_x and ψ_y.

FIG. 4. Ground states $f-j$ of Fig. 1, plotted correspondingly in panels (f)–(j). Displayed quantities are the same as in Fig. 3.

other hand, the corresponding phase difference figures for states g and h show that (i) two vortices, one per component, combine to form one FV in state g, and (ii) four vortices, two per each component, combine to form one skyrmion in state h. The signature of the skyrmion is shown here: four alternating domain walls which are connected into a circular structure [30,31]. The skyrmion state here of course differs from those of magnetic materials due to physics and the formation mechanism [20,32,33]. Nevertheless, their topological properties remain similar, as will be presented later. The phase difference figure of the ground state i shows four DWs around the corners, four HQVs close to the edges, and three FVs in the center. What draws attention in all three contour plots of Fig. 4(i) is that there are five vortices in each component (fractional vortices), and among them three
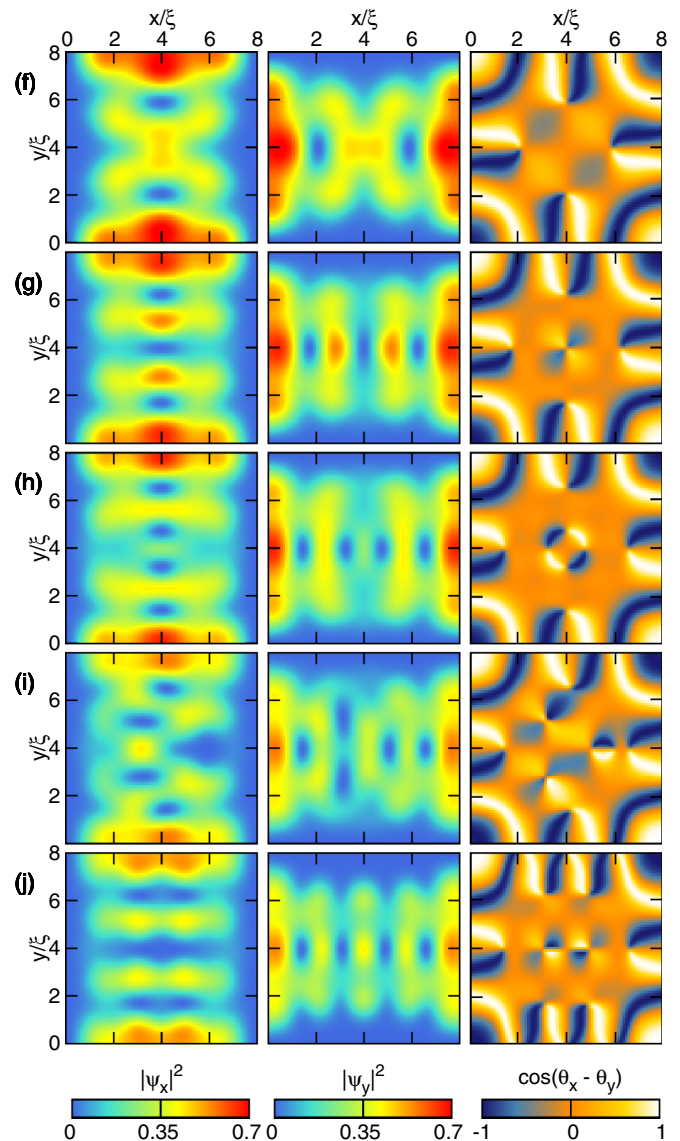
align their cores to form FVs according to the corresponding phase difference figure. The triangular array formed by them resembles the consequences of vortex-vortex repulsion in conventional type-II superconductors. Therefore, this supports our initial premise that the FV in our analysis is the usual Abrikosov vortex of conventional superconductivity. Finally, the phase difference figure of the ground state j shows four DWs, six HQVs, and two FVs. One systematic comparison of the phase difference figure of ground states $f-j$ clearly shows that HQV and FV are indeed very different states. While FVs are formed in the sample center, being favored by confinement, all the HQVs remain close to the sample edges. In order to explain this difference the following subsection discusses the calculated superconducting currents in the sample.

So far, DWs, HQVs, FVs, and skyrmions have been distinguished in this work according to their signatures in the phase difference plots. The superconducting current, the physical quantity intertwined with the magnetic field, also allows us
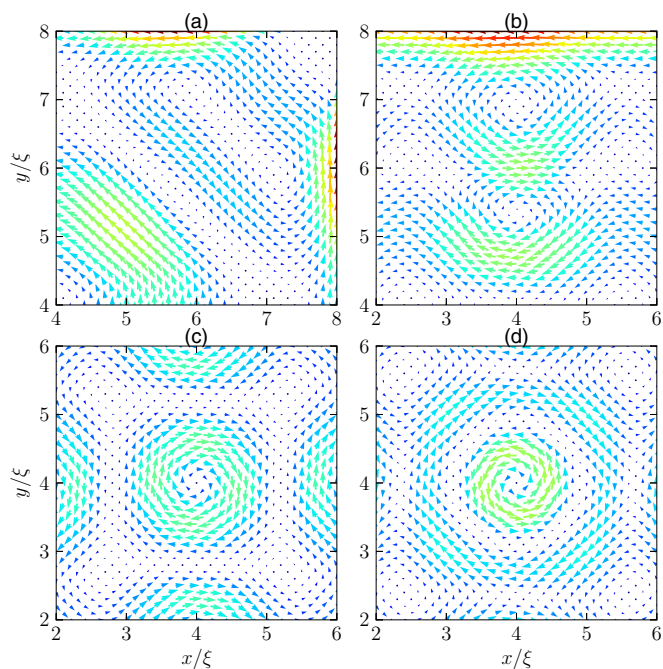
FIG. 5. Superconducting currents around (a) the upper right DW of Fig. 3(c), (b) the upper HQV of Fig. 3(d), (c) the FV of Fig. 4(g), and (d) the skyrmion of Fig. 4(h).

to identify more characteristic features of the topological solutions. Figures 5(a)–5(d) show the supercurrents around one DW, HQV, FV, and skyrmion, respectively. Figure 5(a) zooms in the supercurrents around the right-top DW of Fig. 3(c). One can see two streams flowing in opposite senses at the upper right and lower left corners, respectively. The DW currents arise when these superconducting currents with opposite chiralities meet. In order to understand better the origin of the DW currents, Fig. 6(a) shows the line profiles of the corresponding superconducting densities $|\psi_\pm|^2$ along
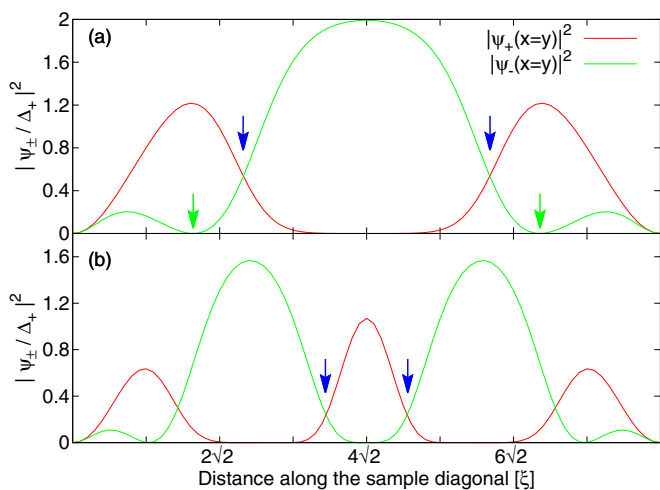

FIG. 6. Diagonal profiles of the contour plots $|\psi_\pm|^2$ corresponding to ground states *c* and *h* of Fig. 1, shown in panels (a) and (b), respectively. Blue and green arrows indicate the DW and vortex core locations, respectively.
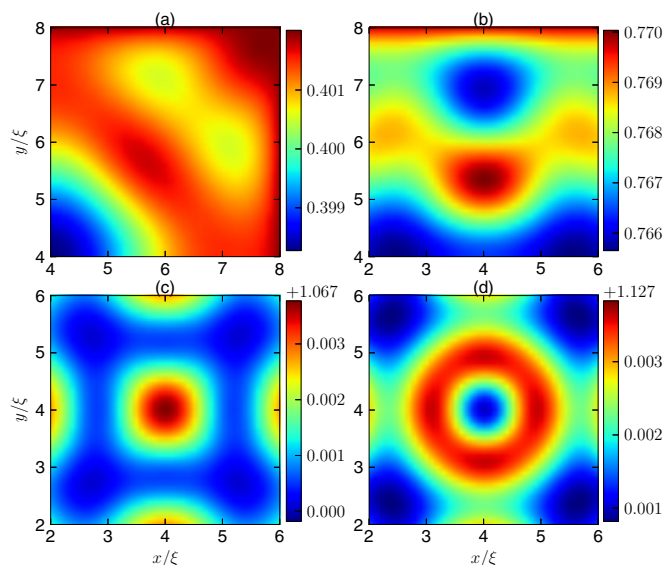

FIG. 7. Contour plots of the magnetic induction corresponding to (a) the supercurrents of the DW of Fig. 5(a), (b) the HQV of Fig. 5(b), the FV of Fig. 5(c), and (d) the skyrmion of Fig. 5(d).

the diagonal line defined by $y = x$. Light (green) arrows point towards the already seen vortex cores of component ψ_- in Fig. 2(c). Dark (blue) arrows indicate the center of two DWs defined by the intersection where the densities $|\psi_-|^2$ and $|\psi_+|^2$ become equal. Where $\psi_+ = 0$, in the center of the sample, the other component (ψ_-) is nonzero and contributes to the chiral superconducting current. On the other hand, where $\psi_- = 0$, ψ_+ is nonzero and its current represents the chiral current flowing close to the corners of the sample.

The magnetic induction that corresponds to the DW supercurrents of Fig. 5(a) is shown in Fig. 7. It is calculated using the Maxwell equation

$$\tilde{\kappa}^2 \nabla \times \vec{B} = \vec{J}, \tag{10}$$

where $\tilde{\kappa}^2 = \kappa^2/d$, with $\kappa = 2.3$ being the GL parameter reported for SRO along the *ab* plane [4], and *d* being the sample thickness which we suitably choose to be 2ξ. The contour plot of Fig. 7(a) shows that the magnetic induction corresponding to the DW is weak and strongly screened by the Meissner effect. This fact represents an obstacle for the detection of DWs signatures in direct measurements of their magnetic response such as in magnetic force microscopy (MFM) or scanning Hall probe microscopy (SHPM).

Figure 5(b) zooms in the supercurrents around the upper HQV of Fig. 3(d). It shows two adjacent counterflowing streams with the bottom one flowing clockwise and belonging to the HQV supercurrents, while the top one flows counterclockwise and represents the screening currents. The Meissner effect for the HQV is anisotropic due to the boundary conditions of Eq. (8). From the supercurrent equation (7), and the local approximation $\psi_y \approx 0$, or $\psi_+ \approx \psi_-$, drawn from Fig. 3(d), one easily obtains $\vec{J} \approx \text{Im}\{\psi_+^* D_x \psi_+ \hat{\imath} + \frac{1}{3} \psi_+ D_y \psi_+ \hat{\jmath}\}$. After straightforward calculations and replacing the covariant derivative once again one obtains $\vec{J} \approx |\psi_+|^2 [(\partial_x \theta \, \hat{\imath} + \frac{1}{3} \partial_y \theta \, \hat{\jmath}) + \frac{Hr}{2}(\sin \phi \, \hat{\imath} - \frac{1}{3} \cos \phi \, \hat{\jmath})]$, which draws attention since the screening currents are defining

elliptical equipotential lines. Thus, the anisotropic screening of the superconductor towards the HQVs causes them to move along the easy-screening direction which in this case is along $\hat{y}$. The contour plot of the magnetic induction corresponding to the supercurrents of Fig. 5(b) is shown in Fig. 7(b). As expected from the two counterflowing streams seen in the HQV supercurrents, the magnetic induction also shows adjacent local maximum and local minimum.

Figure 5(c) zooms in the superconducting currents around the FV of Fig. 4(g), and shows that the FV currents flow clockwise and vanish as we move away from the FV core. This vanishing is due to the spatially isotropic Meissner effect, unlike in a HQV, that screens the FV currents. As expected, its magnetic induction signature [see Fig. 7(c)] agrees well with that of the Abrikosov vortex.

The superconducting currents around the skyrmion of Fig. 4(h) are shown in Fig. 5(d). Unlike the FV, the skyrmion supercurrents clearly show outer and inner structures. The supercurrents of the outer structure flow clockwise while the supercurrents of the inner structure flow counterclockwise. The skyrmionic DW of Fig. 4(h) along with its supercurrents in Fig. 5(d) shows cylindrical symmetry, and one easily deduces that the same symmetry is present in densities $|\psi_{\pm}|^2$. Line profiles of $|\psi_{\pm}|^2$ then provide enough information to unveil the skyrmion supercurrents [see Fig. 6(b)]. The inner structure of the skyrmion is defined by $\psi_- = 0$ and $\psi_+ \neq 0$, i.e., the counterclockwise currents at the core of the skyrmion arise from the chiral component ψ_+. However, away from the skyrmion core the scenario changes since the circular DW of Fig. 4(h) is met, as indicated by arrows in Fig. 6(b). Close beyond the circular DW, we find that while component ψ_+ drops to zero, ψ_- becomes nonzero. Replacing in Eq. (7) $\psi_+ = 0$ and bearing in mind that one giant vortex is hosted in component ψ_-, the supercurrent in cylindrical coordinates becomes $\vec{J} \approx \frac{K+k_1}{4} |\psi_-|^2 (-\frac{2}{r} + \frac{H}{2}r)\hat{\phi}$. The magnetic induction corresponding to the skyrmionic supercurrents of Fig. 5(d) is shown in the contour plot of Fig. 7(d). It clearly shows one local minimum at the skyrmion core surrounded by one circular stripe of local maxima, and as such can be directly imaged in magnetic measurements.

Finally, before concluding this section, we briefly describe the superconducting order parameter $\vec{\Psi}$ in terms of the 3D real vector field $\hat{n}$, defined by [21,34]

$$\hat{n} = \frac{\vec{\Psi}^{\dagger} \hat{\sigma} \vec{\Psi}}{\vec{\Psi}^{\dagger} \cdot \vec{\Psi}}, \quad (11)$$

which maps the complex spaces $\mathbb{C} \times \mathbb{C}$ of components ψ_x, ψ_y into the real space $\mathbb{R}^3$. A straightforward calculation yields $\hat{n} = \sin\alpha\cos\phi, \sin\alpha\sin\phi, \cos\alpha$, where $\sin\alpha = \frac{2|\psi_x||\psi_y|}{|\psi_x|^2+|\psi_y|^2}$, $\cos\alpha = \frac{|\psi_x|^2-|\psi_y|^2}{|\psi_x|^2+|\psi_y|^2}$, and $\phi = \theta_y - \theta_x$. Then, the target space of mapping (11) is the 2D sphere of radius 1, $\mathbb{S}^2$ [35,36]. The topological invariant of the spaces that result from mapping (11) is defined by the integral [20,21]

$$\mathbb{Q} = \frac{1}{4\pi} \int \hat{n} \cdot (\partial_x \hat{n} \times \partial_y \hat{n}) \, dx \, dy, \quad (12)$$

which is widely known as the Hopf invariant. One convenient interpretation of this topological invariant is that it counts the number of times that the 3D real field ($\hat{n}$) wraps around the

2D sphere ($\mathbb{S}^2$). Left and right panels of Fig. 8 show the texture $\hat{n}$ for ground states h and g of Fig. 4, respectively. The texture for the skyrmion (left panel) differs from the texture for the FV (right panel) owing to the alternating circular DW characteristic of the former state. While at the skyrmion core, field $\hat{n}$ points towards $-\hat{j}$, outside the skyrmion it points towards $\hat{j}$. Along the DW that separates the skyrmion core from the outside, the field texture whirls, therefore providing to the space the topological charge $\mathbb{Q} = -2$. The field texture that corresponds to the FV shows a four lobe $C4$ symmetric profile where $\hat{n}$ changes smoothly. Unlike the skyrmion and in agreement with our earlier results, the field texture for the FV does not show any signature of a domain wall separating unequivalent outer and inner regions.

IV. FIELD-DRIVEN TRANSITIONS BETWEEN SKYRMIONIC AND VORTICAL STATES

In bulk and type-II superconducting samples vortices with phase windings higher than $2n\pi$, where n is integer, are energetically disfavored. The superconductor prefers two distant vortices each with phase winding 2π rather than one single vortex (giant vortex) with phase winding 4π. Nevertheless, in samples with dimensions of the order of the superconducting coherence length (mesoscopic samples), giant vortices can appear as stable configurations. The stabilization is provided mainly by the confinement due to the small sample size, although the external magnetic field also contributes through the screening currents and the confining force they exert on vortices. Field driven transitions from states with multiple distant vortices to giant vortices have been widely reported [22,37].

In this section we first report the field-driven transitions from HQV to FV states. Figure 9(a) shows the energy of state f of Fig. 1(a), along with some of its neighboring states. Panel (b) shows the second-order derivative of the energy with respect to the external field only for state f. While the energy of state f is continuous, its second-order derivative shows discontinuities indicating transitions between distinct states. Three different states can be easily distinguished, which we labeled by a circle, square, and triangle marker. The corresponding distributions of the superconducting order parameters are also shown in the figure: logarithmic contour plots of $|\psi_x|^2$ and $|\psi_y|^2$ are shown in the left and central columns, while the cosine of the phase difference is shown in the right column. State ($\bigcirc$) shows two fractional vortices in each component rendering four HQVs according to the phase difference contour plot. State ($\square$) shows two HQVs and two FVs. The FVs are composed of two fractional vortices belonging separately to each component. The fractional vortices composing the FVs are slightly misaligned as can be seen in the density figures. This makes the FVs display a small closed domain wall in the phase difference contour plot. At high fields the screening currents confine even more the superconducting configuration of state ($\square$) transforming it into one state with three HQVs and one FV ($\triangle$). Due to the strong screening currents the upper FV of state ($\square$) loses one of its fractional vortices which renders one HQV in state ($\triangle$). The strong confinement also forces the alignment of the fractional vortices composing the FV of state ($\triangle$).
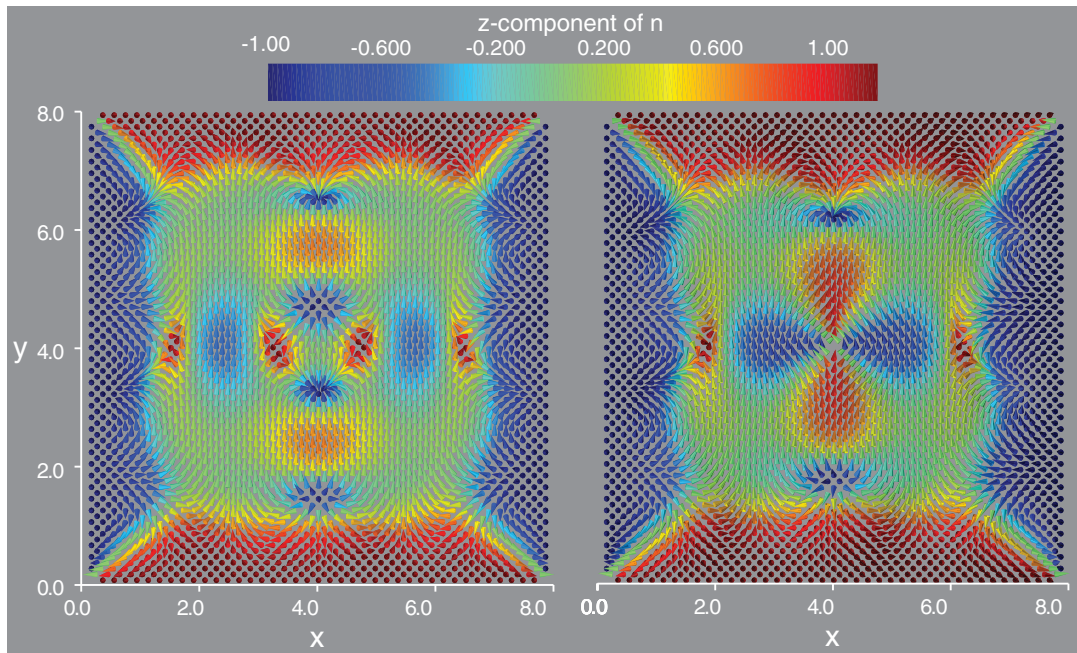
FIG. 8. Textures of the ground states h and g of Fig. 4, according to the mapping $\hat{n} = \vec{\Psi}^{\dagger} \hat{\vec{\sigma}} \vec{\Psi} / \vec{\Psi}^{\dagger} \cdot \vec{\Psi}$, where $\hat{\sigma}$ are the Pauli matrices. Colors show the amplitude of the z component of $\hat{n}$.

Another field-driven transition from skyrmion to FV state is presented in Fig. 10. Panel (a) shows the energy of state j of Fig. 1, along with some of its neighboring states. Panel (b) shows the first- and second-order derivatives of the energy with respect to the external field only for state j. Unlike in Fig. 9(b), here the second derivative is continuous as well as the first derivative. Nevertheless, this does not mean that there are no distinct states along the stability curve of state j. Circle, square, and triangle markers ($\bigcirc$, $\square$, and $\triangle$) indicate three states at weak, intermediate, and strong confinement, respectively. At weak confinement the phase difference figure shows six HQVs and one skyrmion [see Fig. 10 ($\bigcirc$)]. At intermediate confinement, state ($\square$) shows in $|\psi_x|^2$ that two out of the four fractional vortices composing the skyrmion of panel ($\bigcirc$) have merged into one single discontinuity. This merger of initially distant fractional vortices renders the domain wall of the skyrmion asymmetric. At strong confinement ($\triangle$) the former fractional vortices split their cores along the horizontal axis. According to the phase difference figure they join two other fractional vortices in density $|\psi_y|^2$ to form two horizontal FVs in the center of the sample. As can be easily seen, the vorticity of the superconducting components along this field-driven transition is constant, unlike in Fig. 9 where it was not. This fact explains why the second-order derivative is continuous here and discontinuous in Fig. 9.

V. TEMPORAL DYNAMIC TRANSITIONS

Here we benefit from the temporal evolution included in the TDGL equations to report dynamic transitions involving vortices and skyrmions.

The dimensionless free energy as a function of the external field for states i and j is shown in Fig. 11(a). Unlike in Fig. 1 the

sample size here is $12\xi \times 12\xi$ rather than $8\xi \times 8\xi$, which was a suitable choice to study the evolution of the superconducting configuration. Panel (b) shows the temporal evolution of the free energy at the discontinuous step in energy in panel (a). Three states, initial, intermediate, and final, are denoted by circle, square, and triangle markers. The corresponding superconducting order parameters are shown in panels ($\bigcirc$), ($\square$), and ($\triangle$), respectively. The displayed quantities in the latter panels are the same as in those of Fig. 9. The initial state ($\bigcirc$) is a multivortex-skyrmion state containing two pairs of skyrmions and FVs, surrounded by eight HQVs at the sample edges. This state was not obtained for sample size $8\xi \times 8\xi$ mainly due to the strong confinement there. At the intermediate state ($\square$) two fractional vortices nucleate in each component of the superconducting order parameter forming two FVs according to the phase difference contour plot. The four FVs of the intermediate state then combine following the inverse process of the one described in Fig. 10, to form two skyrmions as depicted in state ($\triangle$). In the Supplemental Material [38], we present the animated data showing the temporal evolution of the superconducting order parameter, as a more convenient view of the transition reported here. It is noteworthy here that all field-driven transitions from HQV or skyrmion to FV states and vice versa are essentially driven by HQV penetration and recombination into other topological entities.

Finally we note that the above principles hold also for larger mesoscopic samples, though with more multivortex-skyrmion states found inside the sample, as well as more HQVs at the sample edges. Effectively, the edges of a large mesoscopic sample support realization of the quasi-1D periodic distribution of chiral domains discussed in Ref. [12], with domain walls of length $\approx 3\xi(T)$, i.e., ≈ 600 nm for $T = 0.9T_c$. This length is already matching the limits of scanning SQUID and Hall probe microscopies, explaining why spontaneous currents
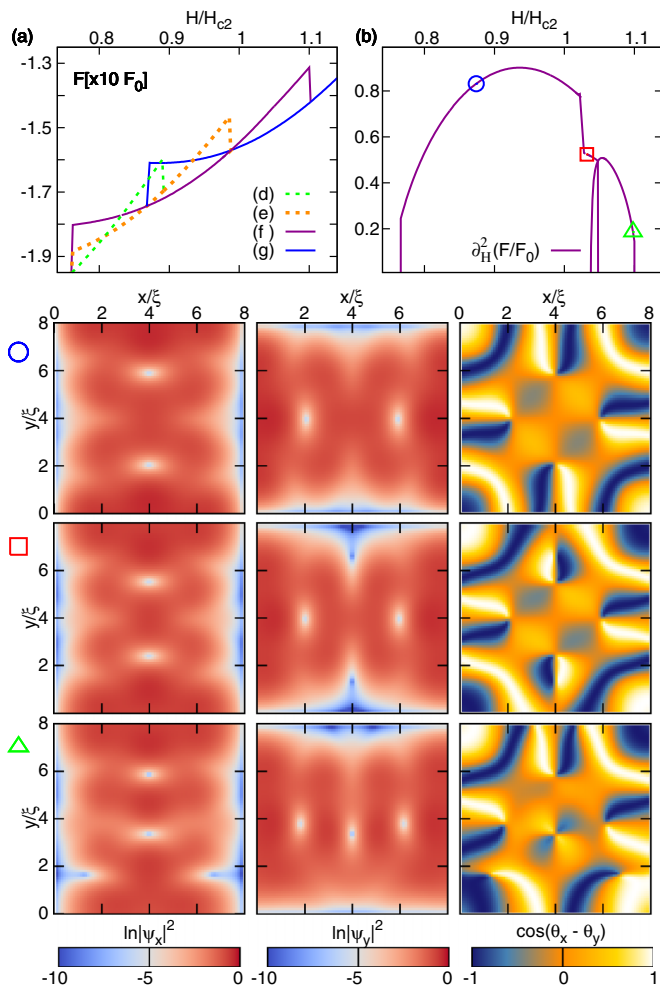
FIG. 9. Field-driven transition from HQV to FV due to confinement in a square mesoscopic sample of size $8\xi \times 8\xi$. (a) Energy of the state f of Fig. 1(a), along with some of its neighboring states. (b) Second-order derivative of the energy with respect to the external field showing three distinct states indicated by circular, squared, and triangular symbols. The corresponding components of the superconducting order parameter are shown in panels ($\bigcirc$), ($\square$), and ($\triangle$). Displayed quantities are logarithmic contour plots of $|\psi_x|^2$ and $|\psi_y|^2$ in left and central columns, respectively, while the cosine of the phase difference is shown at the right column.

remained elusive in experiments to date, always performed on larger samples than considered in this work.

VI. ANISOTROPIC CASE

A. Strong chiral limit

This far, the ground states of a p-wave mesoscopic superconductor with size $8\xi \times 8\xi$ have been obtained under the assumption of weak coupling and with a cylindrical Fermi surface, which led us to set the k_i parameters to $1/3$ [18,27,28]. However, several works have reported or suggested other scenarios for SRO such as (i) multiband superconductivity with the 1D Fermi sheets developing superconducting order [39–42], or (ii) anisotropy in the cylindrical Fermi surface [21,27]. In order to include just anisotropy in the Fermi surface,
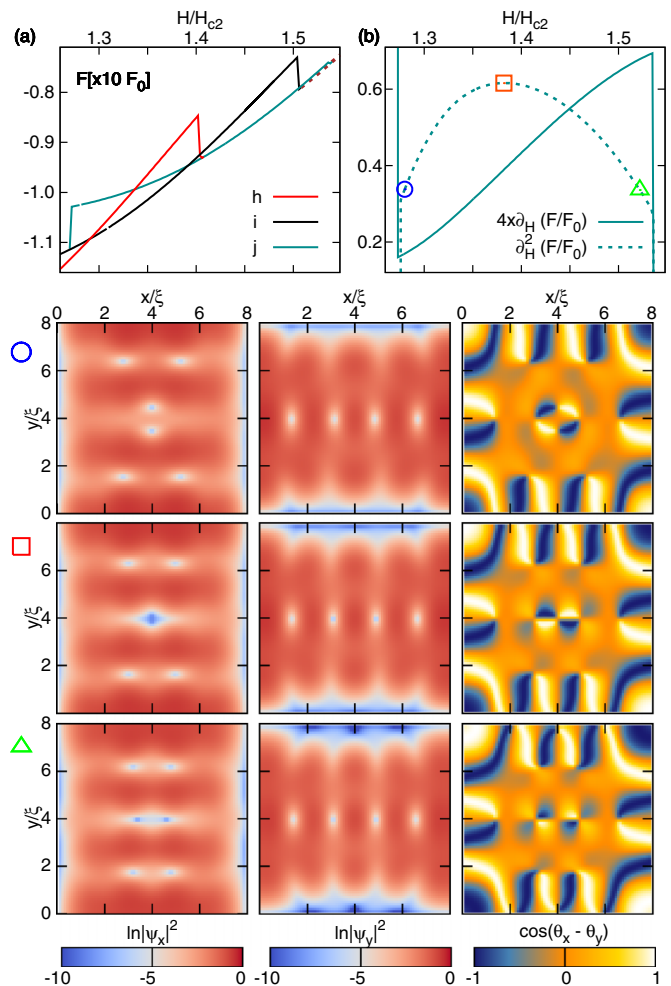
FIG. 10. Another example of a field-driven transition between skyrmionic and vortical states along the state j of Fig. 1. Displayed quantities are the same as in Fig. 9 with the only exception that in panel (b) the first-order derivative of the energy with respect to the external field is also shown.

while preserving single-band superconductivity, and electron-hole symmetry [17,18,29], in this section we introduce the parameter (δ_k), which sets the k_i's to $k_1 = 1/3 + 2\delta_k$, and $k_2 = k_3 = 1/3 - \delta_k$. The motivation behind this choice is that the theoretical values for the k_i parameters corresponding to the three Fermi sheets (γ, α, and β) lie between $1/3 < k_i^\gamma \leqslant 1$ and $0 \leqslant k_i^{\alpha,\beta} < 1/3$ [27], respectively. The GL equation for p-wave superconductors with anisotropy in the Fermi surface becomes

$$\partial_t \vec{\Psi} = \frac{2}{3}[\vec{D}^2 + \Pi_+^2 \hat{\sigma}_+ + \Pi_-^2 \hat{\sigma}_-]\vec{\Psi}$$

$$+ \vec{\Psi}\left(1 - \frac{3|\vec{\Psi}|^2}{4} \pm \frac{\vec{\Psi}^* \hat{\sigma}_z \vec{\Psi}}{4}\right)$$

$$+ \delta_k[\vec{D}^2 - 2(\Pi_+^2 \hat{\sigma}_+ + \Pi_-^2 \hat{\sigma}_-)]\vec{\Psi}. \qquad (13)$$

By tuning δ_k within the interval $[0, 1/3]$, the strength of the nondiagonal (chiral) terms of Eq. (5) is changed, therefore driving the system between two limiting cases, the left limiting case being at $\delta_k = 0$ and given by Eq. (6), and the right limiting
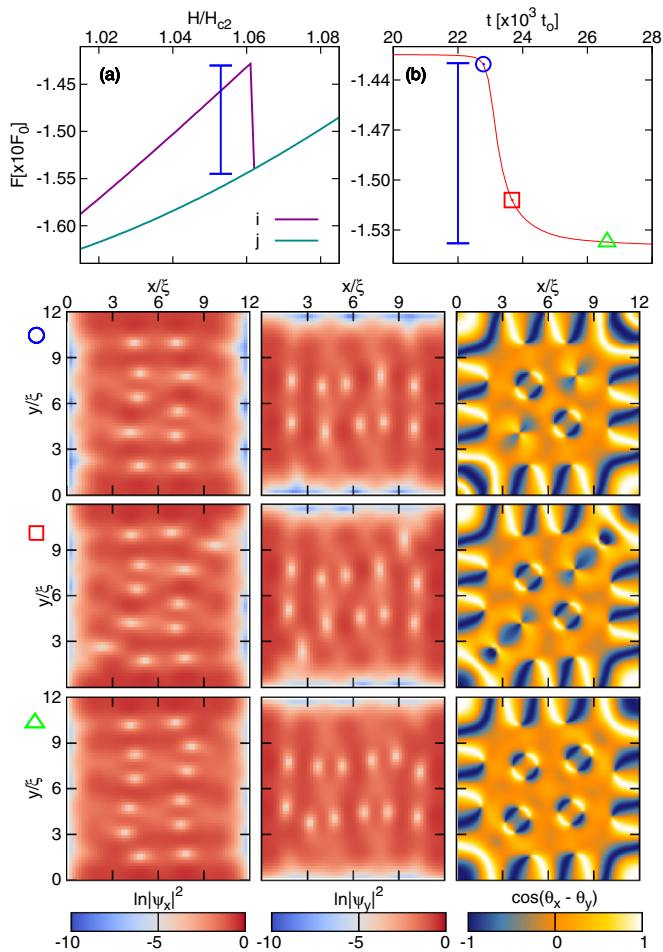
FIG. 11. Temporal vortex-skyrmion transition in a square meso-scopic sample of size $12\xi \times 12\xi$. Panel (a) shows the free energy of states *i* and *j* containing 10 and 12 fractional vortices per component, respectively. The energy of state *i* is discontinuous at $H \approx 1.06H_{c2}$ reflecting a first-order transition. Panel (b) shows the temporal evolution of the energy at the latter transition. Three states, initial, intermediate, and final, are denoted by circle, square, and triangle markers, respectively. The components of the superconducting order parameter corresponding to each state are shown in panels ($\bigcirc$), ($\square$), and ($\triangle$).

case being at $\delta_k = 1/3$ where the chiral coupling between the superconducting components is set to zero.

Figure 12 summarizes the results obtained from the simulations that numerically approach Eq. (13) with $\delta_k = 0.03$. The energy against field plot of Fig. 12 shows nine ground states labeled by letters. The comparison between Figs. 12 and 1 reveals one important fact: the energy of the state *a* is higher than the energy of its adjacent state *b*. Actually, state *a* here is no longer the ground state at low fields $H \approx 0$, unlike in Fig. 1 where it was. Contour plots of the superconducting order parameter ($\vec{\Psi}$) that correspond to states *a* and *b* of Fig. 12 are depicted in insets (a) and (b), respectively. The comparison between the insets of Fig. 12 and the corresponding states in Fig. 2 shows that despite the small anisotropy introduced in the GL equation, the superconducting configuration of these states is practically identical in both cases.
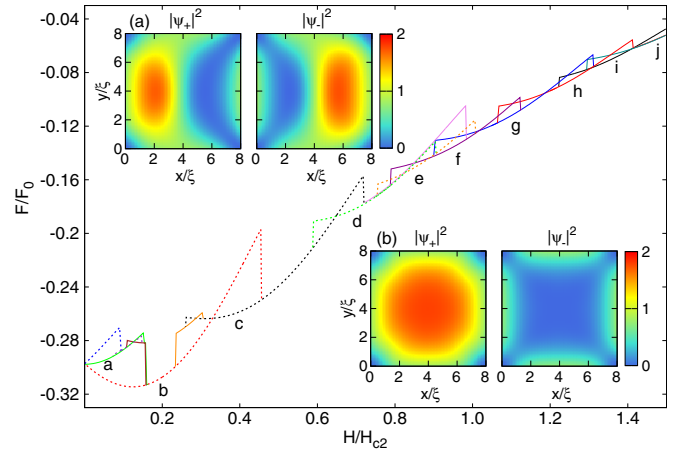

FIG. 12. The free energy as a function of the external magnetic field, showing ground states $b-j$ plus one metastable state *a*, from the numerical simulations using Eq. (13) with $\delta_k = 0.03$. The parameters k_i thus only slightly deviate from the value $1/3$ obtained when a cylindrical Fermi surface is considered. Panels (a) and (b) show the superconducting density components $|\psi_+|^2$ and $|\psi_-|^2$ of the states *a* and *b*, respectively.

Two decades have passed since the discovery of the unconventional properties of strontium ruthenate, but to date there has not been a consensus whether or not it is a chiral *p* -wave superconductor [11,12]. The main experimental results that support unconventional superconductivity in SRO are provided by the set of measurements carried out using techniques such as the Knight shift [6,7], μSR [8], the optical Kerr effect [9], and cantilever magnetometry [24]. The smoking gun evidence that lacks, and which, if found, would convince the scientific community, is the finding of the theoretically predicted spontaneous currents in Sr_2RuO_4 [10,18,43]. Interestingly, what we just found in this work is that the state with spontaneous currents is no longer the ground state when the GL model slightly deviates from the isotropic case at $H \approx 0$, i.e., slightly deviated from the cylindrical Fermi surface. This energy lift of the state with spontaneous currents makes it even harder to be detected. Figure 13(a) shows the supercurrent distribution corresponding to state *a* of Fig. 12. We note that the currents displayed there were obtained at $H = 0$, thus those are the spontaneous currents widely sought in experiments. The spontaneous currents are composed mainly of two counterflowing streams at the left and right sides of our sample. They are the chiral edge currents predicted by Matsumoto and Sigrist [10], Furusaki *et al.* [18], and Stone and Roy [43]. Along the line $x = 4\xi$, the linear domain wall (DW) of Fig. 3(a) separates the left and right sides showing an enhancement in the supercurrents around the center. The magnetic induction corresponding to the supercurrents of panel (a) is shown in panel (b) of the same figure.

Figure 13 shows line profiles of the magnetic induction and the *y* component of $\vec{J}$ along the line $y = 4\xi$. This plot agrees well with the result of Matsumoto and Sigrist which showed that J_y (B_z) is an even (odd) function of *x* along the line perpendicular to the DW [10]. Finally, panels (d) and (e) provide important information that allow us to calculate
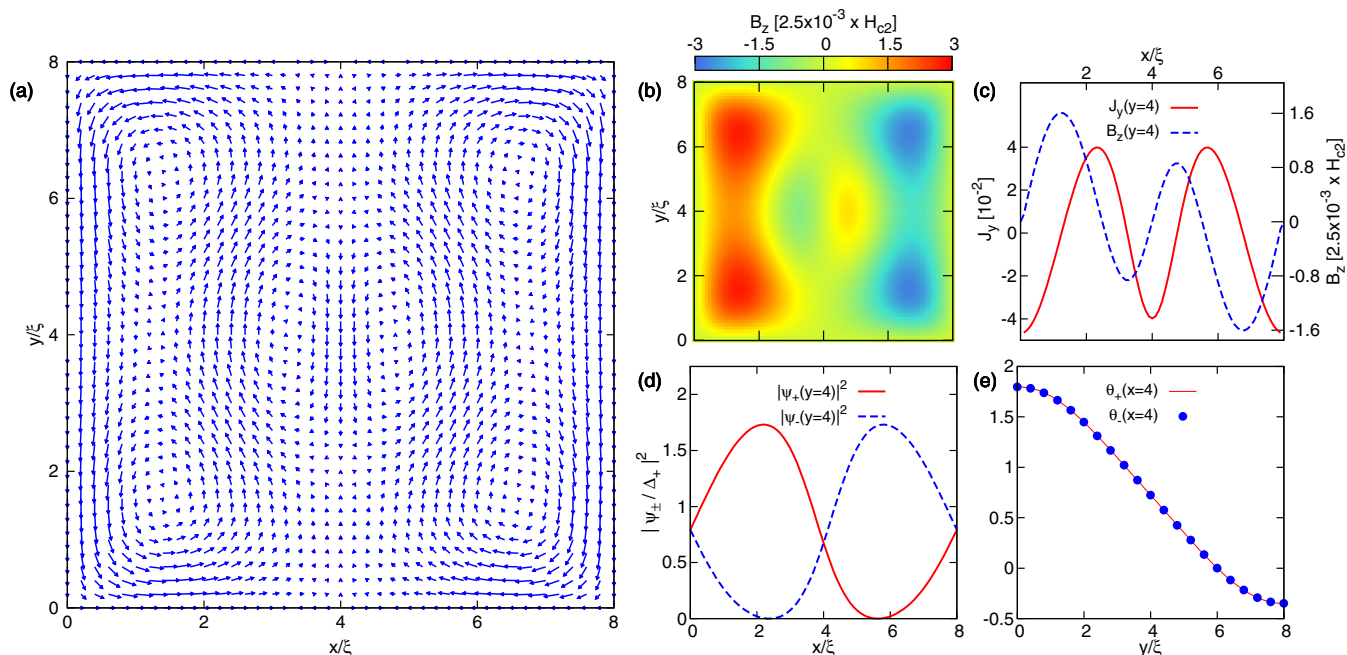
FIG. 13. (a) Superconducting currents corresponding to state a of Fig. 12. These currents, which were obtained at zero field, are composed of two edge currents with different chiralities and flowing in opposite senses. (b) Contour plot of the magnetic induction (B_z) calculated from the supercurrents of panel (a). (c) Line profiles of J_y and B_z along the line $y = 4\xi$. (d) Line profiles of $|\psi_\pm|^2$ corresponding to the state a of Fig. 12. (e) Line profiles of the angular phases of components $\psi_\pm$ along the line $x = 4\xi$.

the supercurrent along the DW. From panel (d) the DW is defined by $|\psi_+| = |\psi_-|$ at $x = 4\xi$, but along this line panel (e) tells us that not only the magnitudes of the superconducting components are equal but also their angular phases. Then, from Eq. (7) our estimation for the superconducting current along the linear domain wall is simply $J_y(x = 4\xi) = k_1|\psi_+|^2\partial_y\theta_+$.

B. Strong Zeeman limit

Microscopy with superconducting quantum interference devices (SQUIDs) and scanning Hall probes (SHPs) have recently detected vortex coalescence in single crystals of strontium ruthenate [13,44]. One possible explanation for this behavior is the existence of at least two different coherence lengths arising from multigap superconductivity, and which lead to attractive (repulsive) interaction at long (short) ranges [41]. References [11] and [13] have reported that within their corresponding resolutions no convincing evidence for spontaneous currents and DWs has been found yet. In order to explore more superconducting configurations, comprising DWs, HQVs, FVs, and skyrmions as the fundamental entities, in what follows a different set of the k_i parameters is defined by $k_1 = 1/3$, $k_2 = 1/3 + \delta_k$, and $k_3 = 1/3 - \delta_k$. Such a choice of parameters enables one to keep constant the strength of the chiral terms while varying δk. The first GL equation for this particular choice of parameters reads

$$\partial_t \vec{\Psi} = \frac{2}{3}\left[\vec{D}^2 + \Pi_+^2\hat{\sigma}_+ + \Pi_-^2\hat{\sigma}_- - \frac{3\delta_k}{2}H\hat{\sigma}_z\right]\vec{\Psi}$$
$$+ \vec{\Psi}\left(1 - \frac{3|\vec{\Psi}|^2}{4} \pm \frac{\vec{\Psi}^*\hat{\sigma}_z\vec{\Psi}}{4}\right). \quad (14)$$

The fourth term in the right side of Eq. (14) represents the orbital Zeeman interaction. It is zero within the weak-coupling limit where $k_2 = k_3$ [18,29]. In this subsection, we consider a possible asymmetry between electron and hole that leads to slightly different k_2 and k_3. In order to study the dependence of the superconducting configuration on the anisotropy parameter, in Eq. (14) the magnetic field is kept fixed while δ_k is varied. Figure 14(a) plots the free energy of the states, solving Eq. (14), as a function of the anisotropy parameter δ_k. Circle, square, and triangle markers denote three states whose $|\psi_+|^2$ and $|\psi_-|^2$ diagonal ($y = x$) line profiles are shown in panels (b) and (c), respectively. From panel (c), and unlike in panel (b), one clearly sees that for high values of δ_k the density $|\psi_-|^2$ diminishes. Our explanation for this behavior is through the definition of two effective coherence lengths, one for each superconducting component. Defining them as the coefficients in front of the linear terms ψ_+ and ψ_- in Eq. (14), they read $\xi_+ = 1 - \delta_k H$ and $\xi_- = 1 + \delta_k H$, respectively. With H fixed and δ_k increasing, ξ_+ (ξ_-) becomes smaller (larger) therefore leading to an effective reduction (increase) of confinement in component ψ_+ (ψ_-). Concerning the phase, contour plots of θ_+, θ_-, and $\cos(\theta_x - \theta_y)$ corresponding to the states denoted by circle, square, and triangle markers are shown in rows (○), (□), and (△). According to the phase difference figure, state (○) is composed of two concentric skyrmions, one circular and one rhomboidal. From the contour plot of θ_- one sees that the circular skyrmion arises from the formation of one giant vortex in ψ_- with phase winding 4π. The phase difference figure corresponding to state (□) shows one irregular closed domain wall emerging from the intersection of the circular and rhomboidal skyrmions. Its formation is determined by the annihilation of the giant vortex in θ_- that has split into
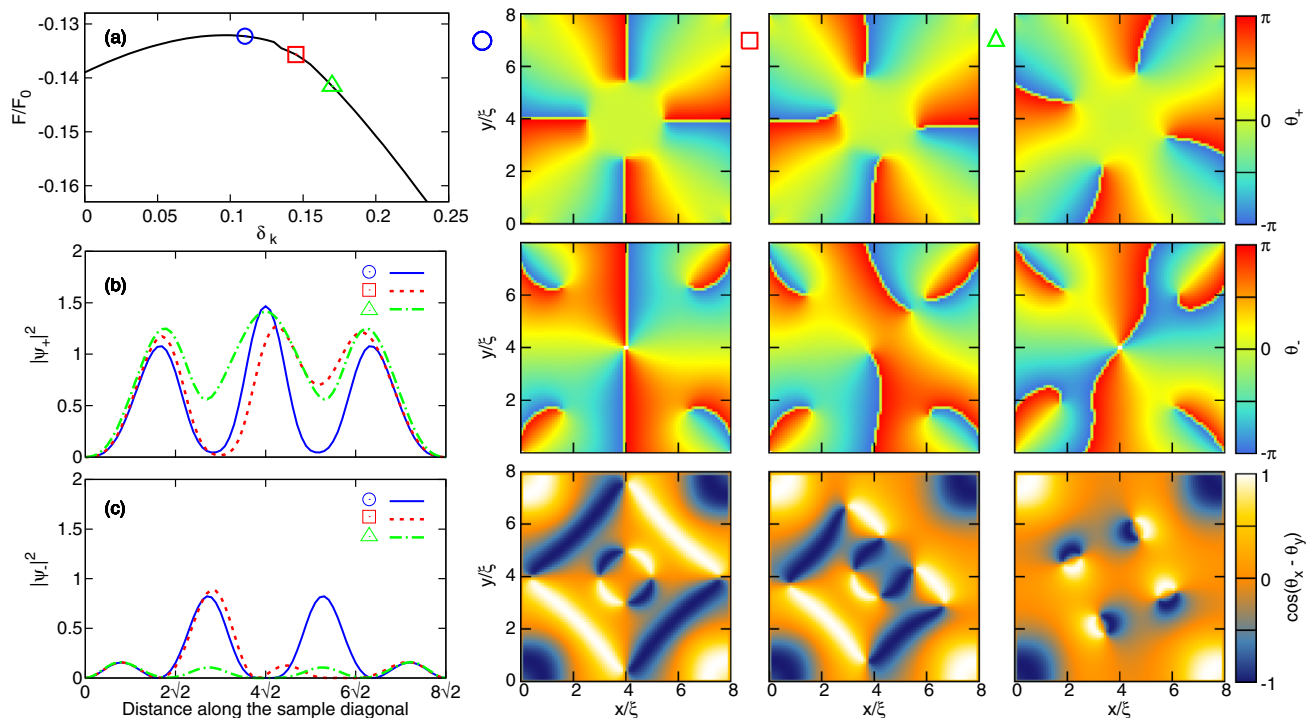
FIG. 14. (a) Free energy as a function of the anisotropy parameter δ_k with the external magnetic field fixed at $H = 0.530[H_{c2}]$. Three distinct states are indicated by circular, square, and triangular markers ($\bigcirc$, $\square$, and $\triangle$). Panels (b) and (c) show line profiles of $|\psi_+|^2$ and $|\psi_-|^2$, respectively, along the diagonal line ($y = x$) corresponding to the states of panel (a). Columns ($\bigcirc$), ($\square$), and ($\triangle$) show contour plots of θ_+, θ_-, and $\cos(\theta_x - \theta_y)$ corresponding to the denoted states of panel (a).

two fractional vortices. Finally, the phase difference figure of state ($\triangle$) shows four FVs with cores slightly asymmetric as can be seen from the small circular DWs present there. Due to the density $|\psi_-|^2$ has been substantially depleted at this value of δ_k, the superconducting state is completely defined by component ψ_+. Hence, what we have achieved by considering asymmetry between electron and hole in the chiral p-wave model of Eq. (5) is a chiral polarization enhanced due to the strong confinement present in a mesoscopic sample.

VII. CONCLUSIONS

In summary, we have studied in detail the Ginzburg-Landau model that describes chiral p-wave superconductors [3,17–19,27,28], and all the possible states of a mesoscopic superconducting sample as a function of the external magnetic field and the anisotropy parameters of the material. Due to odd parity and breaking of the time-reversal symmetry, the order parameter is a two-component complex vector [2,3] and the fundamental solutions of the corresponding TDGL equations, that we obtained numerically, are fractional vortices, i.e., solutions where the phase winding 2π is found in one component but not in the other one. In two- and three-band superconductors similar fractional vortices were obtained between components, but for different reasons [45–47]. Fractional vortices in different components can combine to form a cored/full-vortex state, as well as a coreless/skyrmion state seen in phase difference and magnetic response figures. Skyrmións arise when the same number of fractional vortices in each component combine to form a closed domain wall that

separates distinct intercomponent phase difference ($\theta_x - \theta_y$) regions [30,31]. Alternating segments between 1 and -1 in the $\cos(\theta_x - \theta_y)$ between fractional vortices along the domain wall is the main signature for skyrmions. While for skyrmions the topological charge ($\mathbb{Q}$) is defined by the Hopf invariant [20,21], for vortices it is defined by the circulation of the superconducting velocity. Despite the fact that vector $\vec{d}$ is strongly pinned along $\hat{\mathbf{z}}$ in the chiral representation $\vec{d} = (k_x \pm i k_y)\hat{\mathbf{z}}$ [3,19], we also obtained half quantum vortices analogous to those of spin-triplet superconductors [23]. The screening currents of half quantum vortices are anisotropic and in Cartesian coordinates we have analytically shown that the equipotential lines of the screening currents are ellipsoidal rather than circular as in full vortices. This anisotropic screening causes the attraction of the half quantum vortex towards the sample edges. The mesoscopic size of our samples provides stability to the half quantum vortices and the $\mathbb{Q} = 2$ skyrmions, in contrast to larger systems where larger values of $\mathbb{Q}$ were considered [21], and bulk systems where the half quantum vortices have been usually regarded as high-energy states. Actually the mesoscopic size of the sample plays a remarkable role in the stability of skyrmions as well as in the here reported transitions (e.g., from a skyrmion to a full vortex). At high external fields, above the H_{c1} critical field, states with different configurations of skyrmions and half quantum vortices gradually transform into full vortices owing to the increased screening currents and confinement effects.

To date, the only superconductor expected to be p wave is strontium ruthenate, with enough evidence demonstrating its unconventional behavior [6–9,24]. Nevertheless, many works

have failed to convincingly detect spontaneous currents, half quantum vortices, and skyrmions in large samples [11–13]. What we have demonstrated here is that (i) even by slight anisotropy in the Fermi surface, the state with spontaneous currents is no longer the ground state at $H \approx 0$; (ii) for large mesoscopic samples quasi-1D periodic distribution of chiral domains is realized at the edges of the sample, with half quantum vortices residing on domain walls with a length of several coherence lengths, with magnetic features detectable in scanning SQUID and hall probe microscopy, and (iii)

distinct field-driven transitions between half quantum vortex, full vortex, and skyrmions provide an alternative method to indirectly prove the existence of these exotic states in magnetic measurements.

[1] Y. Maeno, T. M. Rice, and M. Sigrist, Phys. Today **54**(1), 42 (2001).

[2] T. M. Rice and M. Sigrist, J. Phys.: Condens. Matter. **7**, L643 (1995).

[3] M. Sigrist and K. Ueda, Rev. Mod. Phys. **63**, 239 (1991).

[4] A. P. Mackenzie and Y. Maeno, Rev. Mod. Phys. **75**, 657 (2003).

[5] C. Bergemann, A. P. Mackenzie, S. R. Julian, D. Forsythe, and E. Ohmichi, Adv. Phys. **52**, 639 (2010).

[6] K. Ishida, H. Mukuda, Y. Kitaoka, K. Asayama, Z. Q. Mao, Y. Mori and Y. Maeno, Nature (London) **396**, 658 (1998).

[7] H. Murakawa, K. Ishida, K. Kitagawa, Z. Q. Mao, and Y. Maeno, Phys. Rev. Lett. **93**, 167004 (2004).

[8] G. M. Luke, Y. Fudamoto, K. M. Kojima, M. I. Larkin, J. Merrin, B. Nachumi, Y. J. Uemura, Y. Maeno, Z. Q. Mao, Y. Mori, H. Nakamura, and M. Sigrist, Nature (London) **394**, 558 (1998).

[9] J. Xia, Y. Maeno, P. T. Beyersdorf, M. M. Fejer, and A. Kapitulnik, Phys. Rev. Lett. **97**, 167002 (2006).

[10] M. Matsumoto and M. Sigrist, J. Phys. Soc. Jpn. **68**, 994 (1999).

[11] J. R. Kirtley, C. Kallin, C. W. Hicks, E.-A. Kim, Y. Liu, K. A. Moler, Y. Maeno, and K. D. Nelson, Phys. Rev. B **76**, 014526 (2007).

[12] C. W. Hicks, J. R. Kirtley, T. M. Lippman, N. C. Koshnick, M. E. Huber, Y. Maeno, W. M. Yuhasz, M. B. Maple, and K. A. Moler, Phys. Rev. B **81**, 214501 (2010).

[13] P. J. Curran, V. V. Khotkevych, S. J. Bending, A. S. Gibbs, S. L. Lee, and A. P. Mackenzie, Phys. Rev. B **84**, 104507 (2011).

[14] D. A. Ivanov, Phys. Rev. Lett. **86**, 268 (2001).

[15] N. Read and D Green, Phys. Rev. B **61**, 10267 (2000).

[16] S. Das Sarma, C. Nayak, and S. Tewari, Phys. Rev. B **73**, 220502(R) (2006).

[17] J-X. Zhu, C. S. Ting, J. L. Shen, and Z. D. Wang, Phys. Rev. B **56**, 14093 (1997).

[18] A. Furusaki, M. Matsumoto, and M. Sigrist, Phys. Rev. B **64**, 054514 (2001).

[19] S. B. Chung, D. F. Agterberg, and E.-A. Kim, New J. Phys. **11**, 085004 (2009).

[20] N. Nagaosa and Y. Tokura, Nat. Nanotechnol. **8**, 899 (2013).

[21] J. Garaud and E. Babaev, Phys. Rev. B **86**, 060514 (2012); Sci. Rep. **5**, 17540 (2015).

[22] V. A. Schweigert, F. M. Peeters, and P. S. Deo, Phys. Rev. Lett. **81**, 2783 (1998); A. Kanda, B. J. Baelus, F. M. Peeters, K. Kadowaki, and Y. Ootuka, *ibid.* **93**, 257002 (2004); M. V. Milošević, A. Kanda, S. Hatsumi, F. M. Peeters, and Y. Ootuka, *ibid.* **103**, 217003 (2009); B. Xu, M. V. Milošević, S.-H. Lin, F. M. Peeters, and B. Jankó, *ibid.* **107**, 057002 (2011); T. Cren, L. Serrier-Garcia, F. Debontridder, and D. Roditchev, *ibid.* **107**, 097202 (2011).

[23] S. B. Chung, H. Bluhm, and E. A. Kim, Phys. Rev. Lett. **99**, 197002 (2007).

[24] J. Jang, D. G. Ferguson, V. Vakaryuk, R. Budakian, S. B. Chung, P. M. Goldbart, and Y. Maeno, Science **331**, 186 (2011).

[25] M. V. Milošević and R. Geurts, Physica C **470**, 791 (2010).

[26] W. D. Gropp, H. G. Kaper, G. K. Leaf, D. M. Levine, M. Palumbo, and V. M. Vinokur, J. Comput. Phys. **123**, 254 (1996).

[27] D. F. Agterberg, Phys. Rev. Lett. **80**, 5184 (1998).

[28] B.-L. Huang and S.-K. Yip, Phys. Rev. B **86**, 064506 (2012); **87**, 064507 (2013).

[29] M. E. Zhitomirskii, Zh. Eksp. Teor. Fiz. **97**, 1346 (1990) [Sov. Phys. JETP **70**, 760 (1990)].

[30] J. Garaud, J. Carlström, and E. Babaev, Phys. Rev. Lett. **107**, 197001 (2011).

[31] J. Garaud, J. Carlström, E. Babaev, and M. Speight, Phys. Rev. B **87**, 014507 (2013).

[32] P. Milde, D. Köhler, J. Seidel, L. M. Eng, A. Bauer, A. Chacon, J. Kindervater, S. Mühlbauer, C. Pfleiderer, S. Buhrandt, C. Schütte, and A. Rosch, Science **340**, 1076 (2013).

[33] X. Z. Yu, Y. Onose, N. Kanazawa, J. H. Park, J. H. Han, Y. Matsui, N. Nagaosa, and Y. Tokura, Nature (London) **465**, 901 (2010).

[34] E. Babaev, L. D. Faddeev, and A. J. Niemi, Phys. Rev. B **65**, 100512(R) (2002).

[35] E. Babaev, Phys. Rev. Lett. **89**, 067001 (2002).

[36] A. Knigavko and B. Rosenstein, Phys. Rev. Lett. **82**, 1261 (1999).

[37] L. F. Chibotaru, A. Ceulemans, V. Bruyndoncx, and V. V. Moshchalkov, Nature (London) **408**, 833 (2000).

[38] See Supplemental Material at http://link.aps.org/supplemental/10.1103/PhysRevB.93.014518 for animated data showing the temporal evolution of the superconducting order parameter.

[39] K. Deguchi, Z. Q. Mao, H. Yaguchi, and Y. Maeno, Phys. Rev. Lett. **92**, 047002 (2004).

[40] S. Raghu, A. Kapitulnik, and S. A. Kivelson, Phys. Rev. Lett. **105**, 136401 (2010).

[41] J. Garaud, D. F. Agterberg, and E. Babaev, Phys. Rev. B **86**, 060513(R) (2012).

[42] T. Scaffidi, J. C. Romers, and S. H. Simon, Phys. Rev. B **89**, 220510(R) (2014).

[43] M. Stone and R. Roy, Phys. Rev. B **69**, 184511 (2004).

[44] V. O. Dolocan, C. Veauvy, F. Servant, P. Lejay, K. Hasselbach, Y. Liu, and D. Mailly, Phys. Rev. Lett. **95**, 097004 (2005).

[45] L. F. Chibotaru and V. H. Dao, Phys. Rev. B **81**, 020502(R) (2010).

[46] R. Geurts, M. V. Milošević, and F. M. Peeters, Phys. Rev. B **81**, 214514 (2010).

[47] S. Gillis, J. Jäykkä, and M. V. Milošević, Phys. Rev. B **89**, 024512 (2014).